ACS APPLIED MATERIALS & INTERFACES

www.acsami.org Research Article

Selective Valorization of Glycerol to Formic Acid on a $BiVO_4$ Photoanode through NiFe Phenolic Networks

Yiming Han, Mingwei Chang, Zijian Zhao, Fushuang Niu, Zhenghao Zhang, Zehui Sun, Liming Zhang, and Ke Hu*

Cite This: *ACS Appl. Mater. Interfaces* 2023, 15, 11678–11690 Read Online

ACCESS | Metrics & More | Article Recommendations | Supporting Information

ABSTRACT: The integration of the glycerol oxidation reaction (GOR) with the hydrogen evolution reaction in photoelectrochemical (PEC) cells is a desirable alternative to PEC water splitting since a large quantity of glycerol is easily accessible as the byproduct from the biodiesel industry. However, the PEC valorization of glycerol to the value-added products suffers from low Faradaic efficiency and selectivity, especially in acidic conditions, which is beneficial for hydrogen production. Herein, by loading bismuth vanadate (BVO) with a robust catalyst composed of phenolic ligands (tannic acid) coordinated with Ni and Fe ions (TANF), we demonstrate a modified BVO/TANF photoanode for the GOR with a remarkable Faradaic efficiency of over 94% to value-added molecules in a 0.1 M Na_2SO_4/H_2SO_4 (pH = 2) electrolyte. The BVO/TANF photoanode achieved a high photocurrent of 5.26 mA·cm^{-2} at 1.23 V *versus* reversible hydrogen electrode under 100 mW/cm^2 white light irradiation for formic acid production with 85% selectivity, equivalent to 573 mmol/(m^2·h). Transient photocurrent and transient photovoltage techniques and electrochemical impedance spectroscopy along with intensity-modulated photocurrent spectroscopy indicated that the TANF catalyst could accelerate hole transfer kinetics and suppress charge recombination. Comprehensive mechanistic investigations reveal that the GOR is initiated by the photogenerated holes of BVO, while the high selectivity to formic acid is attributed to the selective adsorption of primary hydroxyl groups in glycerol on TANF. This study provides a promising avenue for highly efficient and selective formic acid generation from biomass in acid media *via* PEC cells.

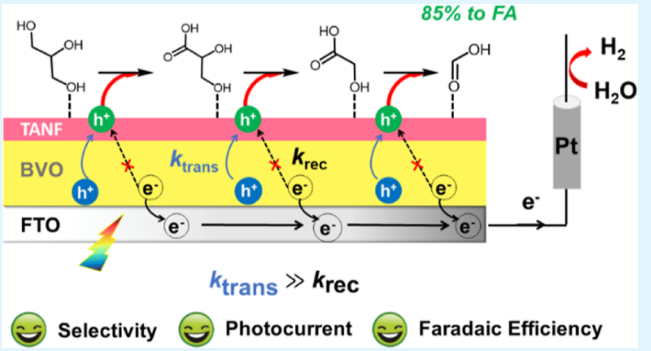

KEYWORDS: *photoelectrochemical cells, glycerol oxidation, formic acid, photoanode, $BiVO_4$*

INTRODUCTION

The pressing climate crisis calls for the development of fuels and building-block chemicals production from renewable resources. Hydrogen energy is a clean and sustainable alternative to fossil fuels. Solar-driven photoelectrochemical (PEC) water splitting provides a promising pathway to producing hydrogen,[1−3] but sluggish kinetics of the oxygen evolution reaction (OER) on the photoanode often limit overall device efficiency.[4−7] Meanwhile, the generation of oxygen gas brings negligible economic benefits. Hence, exploring an alternative photoanode reaction that can generate value-added products is of great interest for the industrial deployment of PEC cells.

Biodiesel, a good substitute for fossil fuel for its good properties and environmental benefits, is now produced in quantities of over 40 million tons per year around the world.[8] Production of 10 pounds of biodiesel results in 1 pound of glycerol as the main byproduct.[9] Efficient utilization of glycerol is a huge potential and profitable market due to the rapid increase of biodiesel consumption. As shown in Scheme 1, glycerol could be transformed into many value-added compounds like dihydroxyacetone (DHA), glyceric acid (GLA), glycolic acid (GLCA), lactic acid (LA), acetic acid (AA), and formic acid (FA).[10] Integrating the hydrogen evolution reaction with the glycerol oxidation reaction (GOR) may achieve better economic returns *via* PEC devices.[11−17]

Apart from the product value, the performance of photoanodes can also be improved by replacing the OER with the GOR. For effective hydrogen production, the anode reaction is best conducted in acidic conditions to maximize the advantages of proton exchange membrane electrolyzers including lower Ohmic losses, higher voltage efficiency, higher current density, and a larger partial load range.[18] The redox

Received: November 15, 2022
Accepted: February 9, 2023
Published: February 21, 2023

https://doi.org/10.1021/acsami.2c20516
ACS Appl. Mater. Interfaces 2023, 15, 11678−11690

Scheme 1. Possible Reaction Pathways for the PEC Glycerol Oxidation

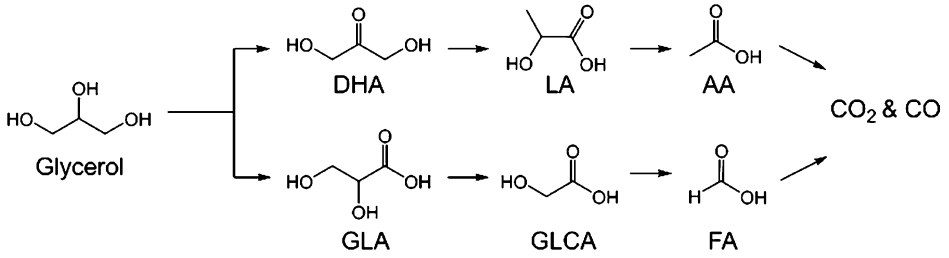

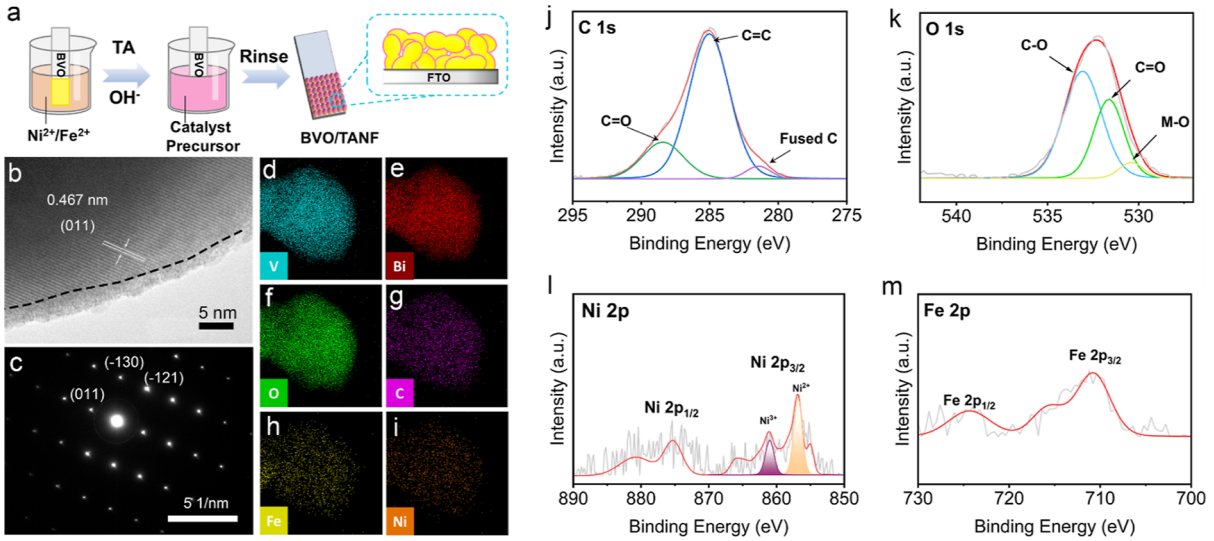

Figure 1. (a) Schematic illustration of the synthesis of the BVO/TANF film. (b) HRTEM image of BVO/TANF. (c) Selected area electron diffraction image of BVO/TANF. STEM−EDS elemental mapping images of BVO/TANF: (d) Bi-L, (e) V-K, (f) O-K, (g) C-K, (h) Ni-K, and (i) Fe-K. XPS spectra of (j) C 1s, (k) O 1s (l) Ni 2p, and (m) Fe 2p.

potential for the GOR is less energy-demanding and could enhance the photon utilization efficiency compared to that of the OER.[19] Some pioneering studies have been reported to achieve selective valorization of glycerol in acid media on semiconductor photoanodes, such as $BiVO_4$ (BVO),[11] Ta:BiVO4,[20] Ag@LDH@TiO_2,[14] and Bi_2O_3/TiO_2.[15] Nevertheless, a satisfactory photocurrent (more than 4 mA·cm^{-2}) or Faradaic efficiency (FE, higher than 80%) was not achieved at low pH conditions. The low FE was probably because the GOR is driven by active hydroxide radicals, leading to the accumulation of H_2O_2[11] and overoxidation of glycerol to CO_2 (Scheme 1).[15] These side reactions also limit the selectivity to the main product for the GOR. Rational design for the photoanode should be conducted to improve the production rate selectivity toward value-added products.

Many studies about the electrochemical GOR have pointed out that earth-abundant metal catalysts showed huge potential in highly selective glycerol valorization, such as nickel−molybdenum−nitride nanoplates (Ni−Mo−N/CFC),[21] Ni-$(OH)_2$,[22] and copper cobalt-based spinel oxide ($CuCo_2O_4$).[23] Inspired by the above studies, we fabricated a low-cost photoanode composed of phenolic ligands (tannic acid, TA) and Ni^{2+}/Fe^{2+} ions (denoted TANF) on porous $BiVO_4$ (BVO). BVO was selected as the visible light harvester for its low production cost, low toxicity, and suitable conduction and valence band energetics for both the GOR and hydrogen generation.[24] The BVO/TANF photoanode displayed a remarkable photocurrent of 5.26 mA·cm^{-2} and an overall FE of 94% toward all value-added products under visible light. With a high production rate of 573 mmol/(m^2·h) toward FA (2 times higher than that of the modified BVO photoanode reported previously),[25] a selectivity as high as 85% for FA in a 0.1 M Na_2SO_4/H_2SO_4 electrolyte (pH = 2) was observed on BVO/TANF, about 2 times higher than that of the unmodified BVO anode in the acidic condition reported previously.[11] Fourier transform infrared (FTIR) spectroscopy and *in situ* infrared reflection absorption spectroscopy (IRRAS) revealed a unique adsorption mode for glycerol on the TANF catalyst overlayer, which is responsible for the observed excellent FA selectivity. Electrochemical and spectroscopic investigations showed that the outstanding PEC performance of BVO/TANF is credited to the enhanced hole transfer kinetics and suppressed charge recombination. Our research discloses the effect of the co-catalyst accelerating the GOR and tuning the reaction pathway on photoanodes, which helps the rational design of PEC devices for efficient biomass valorization coupled with hydrogen production in acidic media.

RESULTS

Photoanode Fabrication and Characterizations. To synthesize monoclinic $BiVO_4$ (BVO), BiOI nanoflake arrays were electrochemically deposited on a fluorine-doped tin dioxide (FTO) substrate. Vanadyl acetylacetonate dissolved in dimethyl sulfoxide (DMSO) reacted with BiOI nanoflakes at programed temperatures according to the previous reports.[11,26] The crystallinity of the BVO thin film was confirmed by X-ray diffraction (XRD, JCPDS PDF 14-0688, Figure S1). Scanning electron microscopy (SEM) showed that the as-prepared

https://doi.org/10.1021/acsami.2c20516
ACS Appl. Mater. Interfaces 2023, 15, 11678−11690

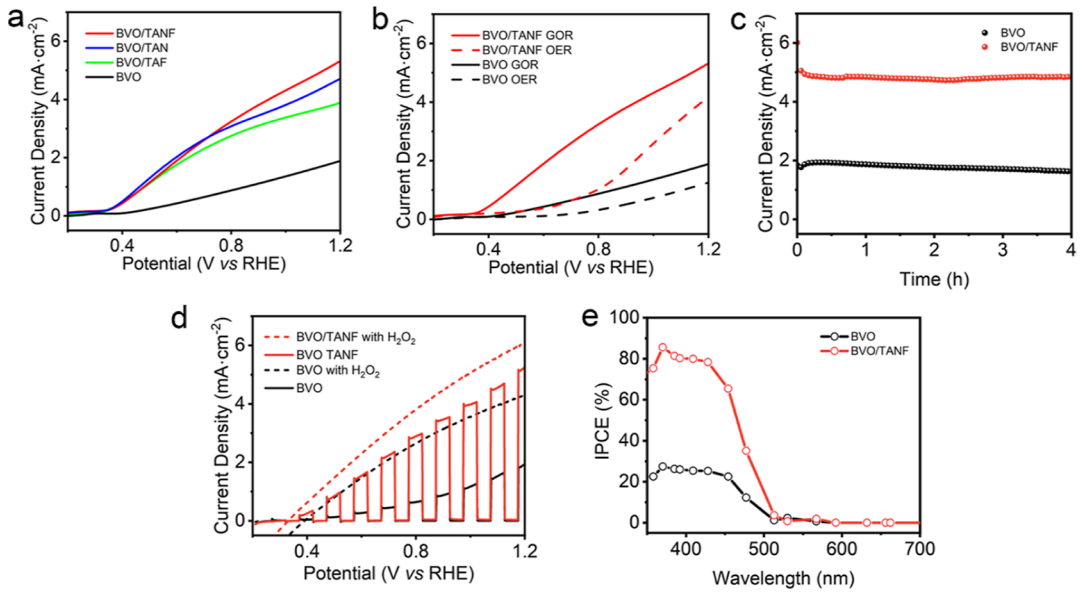

Figure 2. Linear sweep voltammograms of (a) GOR tests on different photoanodes. (b) GOR and OER tests on BVO and BVO/TANF photoanodes under white light illumination (100 mW·cm^{-2}). Electrolyte: 0.1 M Na_2SO_4/H_2SO_4 (pH = 2) with or without 0.1 M glycerol for the GOR and OER tests, respectively. (c) J−t curves measured in an electrolyte with 0.1 M glycerol under white light illumination (100 mW·cm^{-2}). (d) Chopped LSV curves of BVO and BVO/TANF with 0.1 M glycerol or with 0.1 M H_2O_2. (e) IPCE spectra of BVO and BVO/TANF with 0.1 M glycerol.

$BiVO_4$ photoanode comprised interlaced nanoporous arrays, with a mean particle size of ∼100 nm (Figure S2a) and a thickness of ∼400 nm (Figure S2b). The NiFe phenolic co-catalyst was loaded on the BVO photoanode according to the previous work through a simple solution reaction, where metal ions were immobilized with TA on the BVO surface under a weak alkaline solution.[27,28] UV−vis diffuse reflectance spectroscopy (DRS, Figure S3a) displayed clear characteristic adsorption of the Fe−TA coordination complex between 500 and 700 nm on BVO/TANF.[29] Attenuated total reflectance (ATR) FTIR spectroscopy was also conducted on BVO and BVO/TANF to confirm the existence of metal phenolic networks (Figure S3b). The peaks of carbonyl groups (1700 cm^{-1}), aromatic rings (1570−1450 cm^{-1}), and C−O bonds (1325 and 1204 cm^{-1}) were observed on the difference spectra generated by subtracting the spectrum measured on BVO from the spectrum measured on BVO/TANF, which could be assigned to the TA molecules in the co-catalyst.[30−32] No significant difference was found between BVO and BVO/TANF from SEM and XRD (Figures S1 and S4a,b). Thus, high-resolution transmission electron microscopy (HRTEM) was conducted further to examine the morphology of BVO/TANF (Figures 1b and S4c,d). The TANF coating compactly covered the surface of $BiVO_4$ nanoparticles (NPs) (Figure S4c,d). A thickness of 2.5 nm was discovered for the TANF co-catalyst, as shown in Figure 1b. A well-formed monocrystal with the interplanar spacing of 0.467 nm was observed for the covered BVO NP, consisting of the (011) plane of monoclinic $BiVO_4$ (Figure 1b). The separations of 0.467, 0.312, and 0.309 nm in the selective area electron diffraction (SAED) patterns (Figure 1c) corresponded to the distances between (011), (−130), and (−121) crystal planes of monoclinic $BiVO_4$, respectively. The scanning transmission electron microscopy-energy-dispersive X-ray spectroscopy (STEM-EDS) elemental mapping images indicated the uniform distribution of Bi, V, O, C, Ni, and Fe elements in the whole region of the BVO/TANF nanostructure (Figure 1d−i). It was demonstrated that the metal−TA co-catalyst was successfully modified to the surface of the BVO photoanode.

X-ray photoelectron spectroscopy (XPS) was conducted on different photoanodes to determine their elemental compositions (Figures 1j−m and S5a−f). Characteristic peaks for the C═C bond and C═O bond in the phenolic network were observed in the C 1s signals (Figure 1j). For the O 1s signals, BVO/TANF displayed three peaks at 533.2, 531.6, and 530.4 eV (Figure 1k), respectively, assigned to the C−O bond, C═O bond, and metal−O bond in the TANF network (Figure 1k). Compared to that in bare BVO, the peaks of Bi 4f (159.2 and 164.4 eV) and V 2p (516.8 eV) in the BVO lattice decreased greatly in BVO/TANF (Figure S5a,b). For the O 1s spectra, the pristine BVO displayed two typical peaks at 531 eV (hydroxyl groups bonded to the metal cations) and 528.8 eV (lattice O^{2-}, Figure S5c),[33] which were not observed on BVO/TANF. Considering the thickness of ∼2.5 nm for TANF, it was indicated that the BVO NPs were well-wrapped by TANF, leading to the reduced XPS signals of lattice BVO. The intimate interaction of BVO and TANF might come from catechol groups in TA, which could coordinate spontaneously and strongly with metal atoms.[34,35] The XPS Ni $2p_{3/2}$ peak located at 856.8 eV indicated that Ni has an oxidation state of +2 in TANF, while the peak located at 861.0 eV was attributed to the peak of Ni^{3+} (Figure 1l).[36,37] It was difficult to fit the weak signals of Fe 2p and determine the oxidation state (Figure 1m), which was also reported in a previous work.[38]

Besides BVO/TANF, we also prepared BVO photoanodes modified by Ni phenolic (BVO/TAN) and Fe phenolic (BVO/TAF) networks as control samples, respectively. Stronger signals of Ni $2p_{1/2}$ and Ni $2p_{3/2}$ peaks were found on BVO/TANF BVO/TAN (Figure S5d). According to prior reports, the Fe^{2+}−TA film was thicker than the Ni^{2+}−TA film in the same deposition condition.[39] It was implied that Fe^{2+} accelerated the deposition speed of the co-catalyst and

https://doi.org/10.1021/acsami.2c20516
ACS Appl. Mater. Interfaces 2023, 15, 11678−11690

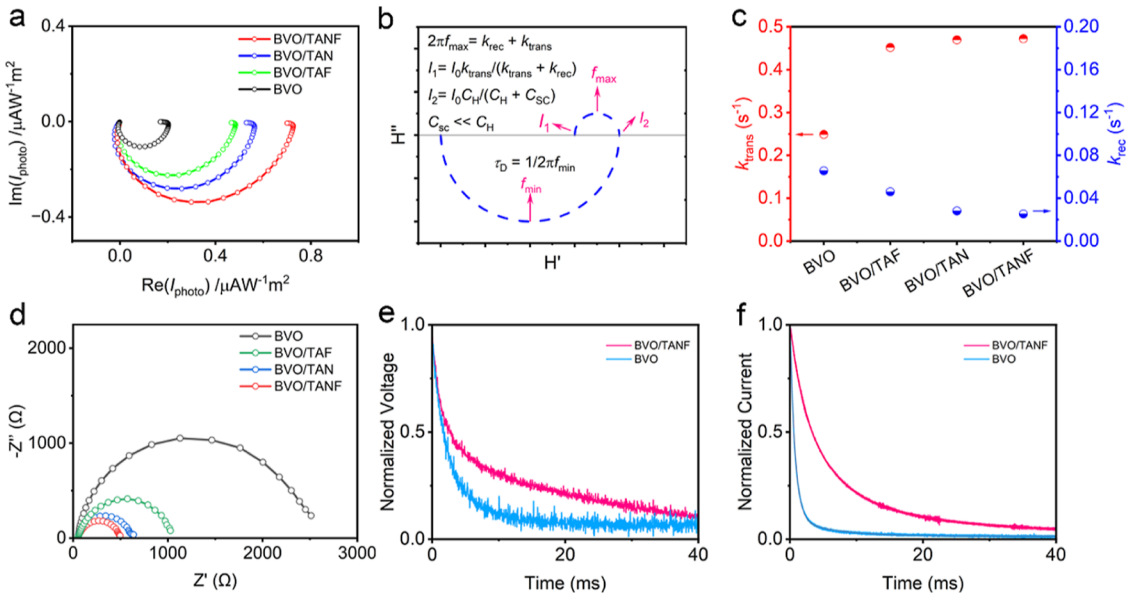

Figure 3. (a) IMPS spectra of different photoanodes. (b) Calculated example of the IMPS spectrum. (c) Calculated k_{trans} and k_{rec} values of different photoanodes. (d) EIS spectra of different photoanodes. (e) TPV and (f) TPC curves of BVO and BVO/TANF.

increased the amount of both Ni^{2+} and Fe^{2+} irons, leading to the stronger signals of the Ni element for BVO/TANF. Stronger peaks of O 1s and C 1s were also found on BVO/TANF than on BVO/TAN (Figure S5e,f), which corresponded to the well-deposited metal phenolic networks for BVO/TANF.

PEC Performance. The PEC performance of various photoanodes was investigated in 0.1 M Na_2SO_4/H_2SO_4 solution with a pH of 2 under 100 mW·cm^{-2} white light illumination (the theoretical maximized photocurrent density of bare BVO is 8.5 mA·cm^{-2} according to our calculation from the emission spectrum of the LED lamp). Both BVO/TAN and BVO/TAF demonstrated lower current density than BVO/TANF but still higher current density than pristine BVO (Figure 2a). The chopped J–t test also showed this tendency, indicating that the presence of both Ni and Fe in the metal phenolic network is necessary for high current density (Figure S6). Then, we focused on the difference in PEC activity between BVO and BVO/TANF. Figure 2b displays the current density–potential profile of BVO and BVO/TANF for the OER and GOR, in which a larger current density was observed on both BVO and BVO/TANF after the addition of glycerol. Meanwhile, the current density of BVO-based photoanodes increased more quickly on the linear sweep voltammetry (LSV) curves at a low bias region [0.4–0.8 V *vs* reversible hydrogen electrode (RHE), Figure 2b]. It implies that the GOR was more favorable than the OER in acidic conditions.[11] The highest photocurrent of 5.26 mA·cm^{-2} at 1.2 V *versus* RHE was achieved on BVO/TANF, which is 2.8 times higher than that of bare BVO (1.88 mA·cm^{-2}). At the same time, the onset potential for the GOR shifted from 0.20 V *versus* RHE for pristine BVO to 0.07 V *versus* RHE for BVO/TANF (Figure S7a). Unsatisfactory stability was observed for the OER on both BVO and BVO/TANF (Figure S7b). Adding glycerol into the electrolyte improved the stability of both BVO and BVO/TANF photoanodes. A moderate photocurrent decay for the GOR was observed on bare BVO under long-time irradiation for 4 h (Figure 2c, from ~2.0 to 1.5 mA·cm^{-2}). However, BVO/TANF displayed excellent stability with a photocurrent of about 5 mA·cm^{-2} after 4 h (Figure 2c).

To better understand the PEC performance of BVO and BVO/TANF films, linear sweep voltammograms with 0.1 M glycerol or with 0.1 M hole scavenger (hydrogen peroxide) were obtained on both BVO and BVO/TANF to evaluate the surface charge transfer efficiency η_{ct} associated with the surface reaching holes that are injected into the solution species

$$\eta_{ct} = \frac{J_{GOR}}{J_{H_2O_2}} \quad (1)$$

where J_{GOR} is the current density of the GOR and $J_{H_2O_2}$ is the current density of the photoanode in the electrolyte containing H_2O_2. Pristine BVO displayed a photocurrent of 4.3 mA·cm^{-2} at 1.2 V *versus* RHE in 0.1 M Na_2SO_4/H_2SO_4 solution (pH = 2) with H_2O_2 as the electron donor, which is 2.2 times higher than that of the GOR (η_{ct} = 44.8%, Figure 2d). However, on the modified photoanodes, the η_{ct} was significantly increased (86.5% for BVO/TANF at 1.2 V *vs* RHE). The high η_{ct} value of BVO/TANF showed that charge recombination on the BVO/TANF photoanode surface was vastly suppressed compared to that on BVO. Under low bias conditions (around 0.4 V *vs* RHE), a sharp decline of the photocurrent appeared after the illumination for bare BVO. On the contrary, the modified photoanodes displayed ascending photocurrent with increasing applied bias. The ascending photocurrent of BVO/TANF after illumination indicated that photogenerated holes could be consumed quickly through the GOR instead of a loss in charge recombination, in agreement with the η_{ct} calculation result. Incident photon-to-current conversion efficiency (IPCE) spectra were collected for both BVO and BVO/TANF at 1.2 V *versus* RHE in 0.1 M Na_2SO_4/H_2SO_4 (pH = 2) solution containing glycerol (Figure 2e). The IPCE curves demonstrated that BVO/TANF manifested an excellent IPCE of ~80% from 400 to 450 nm, whereas the IPCE values for pristine BVO were lower than 30% in this range. Though BVO/TANF could adsorb the photons of long wavelengths in the visible region (revealed by DRS spectra, Figure S3), no

https://doi.org/10.1021/acsami.2c20516
ACS Appl. Mater. Interfaces 2023, 15, 11678–11690

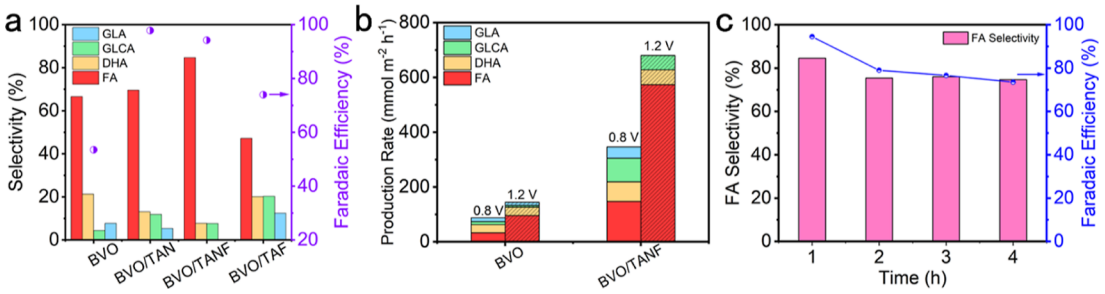

Figure 4. (a) Selectivity and FE of different photoanodes for the GOR at 1.2 V *vs* RHE. (b) Production rate of BVO and BVO/TANF at 0.8 or 1.2 V *vs* RHE. (c) Long-term selectivity and FE of BVO/TANF at 1.2 V *vs* RHE. Electrolyte: 0.1 M Na_2SO_4/H_2SO_4 solution (pH = 2) with 0.1 M glycerol.

obvious discrepancies were found between the IPCE spectra of BVO/TANF and pristine BVO. Hence, the improvement of the PEC efficiency is unlikely to be the result of more light being absorbed but rather surface kinetics related to the charge transfer and/or catalytic pathways.

Electrochemical Spectroscopy. Intensity-modulated photocurrent spectroscopy (IMPS) characterizations were carried out to investigate the hole transfer kinetics from the bulk to surface for different photoanodes. Figure 3a shows a complex plane plot of the IMPS spectrum for BVO, BVO/TAF, BVO/TAN, and BVO/TANF at 1.2 V *versus* RHE in the GOR condition. In the Nyquist plot, each photoanode displayed two semicircles, which corresponded to the resistance−capacitance attenuation and the competition between charge transfer and recombination, respectively. A calculated example of the IMPS spectrum for various kinetics properties is shown in Figure 3b.[40] In the IMPS technique, the perturbed photocurrent $j(\omega)$ is expressed as

$$\frac{j_{photo}(\omega)}{j_h(\omega)} = \frac{k_{trans} + i\omega\frac{C}{C_{sc}}}{k_{trans} + k_{rec} + i\omega}\left(\frac{1}{1 + i\omega RC}\right) \quad (2)$$

$$C = \frac{C_{sc}C_H}{C_{sc} + C_H} \quad (3)$$

where $j_h(\omega)$ is the periodic flux of photogenerated holes corresponding to the Gärtner equation, k_{trans} is the charge transfer rate constant, k_{rec} is the charge recombination rate constant, C is the effective capacitance, C_{SC} is the space−charge capacitance, R is the total series resistance, ω is the light modulation frequency, and C_H is the Helmholtz capacitance. Generally, the Helmholtz capacitance is much larger than space−charge capacitance ($C_{sc} \ll C_H$), so I_0 approximately equals the value of the intercept at high frequency [I_2, $I_2 = I_0C_H/(C_H + C_{sc})$]. Hence, the upper semicircle can be used to determine k_{trans} and k_{rec} from the frequency at the summit ($2\pi f_{max} = k_{trans} + k_{rec}$) and the intercept at low frequency with the real axis I_1 ($I_1 = I_0k_{trans}/(k_{trans} + k_{rec}) \approx I_2k_{trans}/(k_{trans} + k_{rec})$),[41] as shown in Figure 3b. The k_{trans} and k_{rec} values of different photoanodes in the GOR are displayed in Figure 3c. At the applied bias of 1.2 V *versus* RHE, the k_{trans} of modified photoanodes (BVO/TAN, BVO/TANF, and BVO/TAF) surpassed that of pristine BVO for the GOR by a factor of 1.8−1.9. Among them, BVO/TANF had the largest k_{trans} of 0.472 s^{-1}. At the same time, k_{rec} of BVO was 0.065 s^{-1}, which was 1.42, 2.32, and 2.58 times as large as those of BVO/TAF (0.046 s^{-1}), BVO/TAN (0.028 s^{-1}), and BVO/TANF (0.025 s^{-1}), respectively. The BVO/TANF photoanode had the highest k_{trans}/k_{rec} value, corresponding to its best GOR performance among all investigated photoanodes. Note that the η_{ct} value could also be calculated from $\eta_{ct} = k_{trans}/(k_{trans} + k_{rec})$, and the η_{ct} values obtained from the IMPS spectra (Table S1) were higher than the values obtained from hole scavenger measurements. The higher η_{ct} values may be caused by the nonlinearity of measurements in the photocurrent with respect to the light intensity.[42] Also, the higher η_{ct} values from IMPS than that from the other method have been reported previously.[43] Hence, we selected the η_{ct} values from the hole scavenger measurements in our work. The frequency at the nadir of the semicircle (f_{min}) can be utilized to determine the time constant of the hole transfer inside the electrodes. The average time photogenerated holes need to reach the surface of photoanodes, the transit time τ_D, can be estimated from $\tau_D = (2\pi f_{min})^{-1}$. The time scale of τ_D corresponds to the result of the k_{trans} calculation. BVO/TANF displayed smaller τ_D at any applied bias than BVO, indicating faster hole transfer from BVO to the TANF co-catalyst (Figure S8).

We then turned to electrochemical impedance spectroscopy (EIS) to better understand the surface charge transfer for the GOR of different photoanodes (Figure 3d). The EIS data were collected under visible light irradiation at 1.2 V *versus* RHE. All photoanodes displayed semicircles in the Nyquist plots, which were analyzed through an equivalent circuit (shown in Figure S9, the results of the simulation are listed in Table S2) consisting of series resistance (R_s), charge transfer resistance (R_{ct}), and C_{sc}. The smaller radius of the EIS curve revealed lower R_{ct}, indicating faster charge transfer. The obtained trend of the R_{ct} values was as follows: BVO/TANF < BVO/TAN < BVO/TAF < BVO. BVO/TANF displayed the lowest R_{ct} of 407.2 Ω in all photoanodes, which was 5.57 times lower than that of bare BVO. An obvious difference in R_s values was not observed, which suggested that the bulk charge transfer inside BVO-based materials hardly changed. We also found that BVO/TANF had larger C_{sc} than BVO, BVO/TAF, and BVO/TAN (Table S2), suggesting a higher electrochemical surface area on BVO/TANF.

We further conducted transient photocurrent/transient photovoltage (TPC/TPV) measurements to investigate the lifetimes of trapped holes and the rate of charge transfer.[44,45] Figure 3e,f displays the TPV and TPC curves of BVO and BVO/TANF. Both TPC and TPV signals could be illustrated in terms of two time constants (τ_1 and τ_2) and probability constants (φ_1 and φ_2),[44] as listed in Tables S3 and S4. The probability-weighted average decay time ($\bar{\tau}$) of TPV decay curves is indicative of the average charge recombination kinetics of photoanodes.[46] BVO/TANF displayed a $\bar{\tau}$ value of

https://doi.org/10.1021/acsami.2c20516
ACS Appl. Mater. Interfaces 2023, 15, 11678−11690

20.9 ms, 6.9 times higher than that of pristine BVO (3.02 ms). The fast kinetic component (related to τ_1) was dominant in pristine BVO ($\varphi_1 = 0.638$), while in BVO/TANF, the φ_1 value was only 0.241. For the moment, the TPC curves can reveal the electron transit time ($\overline{\tau}'$) from the semiconductor to the FTO substrate.[47] The time constants of BVO and BVO/TANF photoanodes showed a similar trend to the TPV tests. A longer average carrier lifetime ($\overline{\tau}' = 5.95$ ms) was observed than that of bare BVO ($\overline{\tau}' = 1.06$ ms).

Intermediate and Product Analysis. The GOR product analysis after 1 h irradiation for the BVO, BVO/TAF, BVO/TAN, and BVO/TANF photoanodes was conducted in 0.1 M Na_2SO_4/H_2SO_4 solution (pH = 2) with 0.1 M glycerol at 1.2 V *versus* RHE. The reaction products on these photoanodes included FA, DHA, GLCA, and GLA, which were quantified by high-performance liquid chromatography (HPLC). Figure 4a displays the selectivity of different BVO-based photoanodes for various products. The BVO/TAF anode achieved higher selectivity to C2−C3 molecules than other anodes (Figure 4a) with a modest FE of 72% to organic species, better than the FE of BVO (~50%). BVO/TAN and BVO/TANF showed a high FE of over 94% for all liquid products, and BVO/TANF displayed the highest selectivity of 85% toward FA (Figure 4a). CO and oxygen were also detected as side products by gas chromatography for the GOR on BVO/TANF. We then examined the GOR liquid products of BVO and BVO/TANF at different bias voltages (0.8 and 1.2 V *vs* RHE). Pristine BVO displayed a similar selectivity of 66% toward FA and a low FE of ~50% to overall organic products at both 0.8 and 1.2 V *versus* RHE (Figures 4a and S10). Compared to BVO, more GLCA and GLA molecules were generated at 0.8 V *versus* RHE for BVO/TANF. The generation of DHA and GLCA was inhibited at 1.2 V *versus* RHE for BVO/TANF, leading to an excellent selectivity of 85% toward FA with a production rate of 573.3 mmol·m^{-2}·h^{-1} (Figures 4b and S10). Hence, 1.2 V *versus* RHE was chosen as the applied bias in further tests. The hydrogen production rate was determined by gas chromatography. An FE of over ~93% for hydrogen production was maintained on a long-time scale (Figure S11). Under a long-term GOR test for 4 h, the selectivity to FA decreased to 75% with an FE of 76% for all organic products (Figure 4c).

To gain further insights into the role of the photogenerated holes and radicals in the GOR, quenching experiments were carried out on the BVO/TANF anode. Adding $K_2S_2O_8$ (photoelectron scavenger) and *tert*-butanol (hydroxyl radical scavenger) had little effect on the FA production rate (Figure S12a,b). Meanwhile, after adding Na_2SO_3 (hole scavenger) to the electrolyte, the conversion rate from glycerol to FA decreased greatly (Figure S12a,b). These results suggest that the GOR may be driven by holes. To detect the possible generated radicals during the GOR, we conducted matrix-assisted laser desorption ionization time of flight mass spectrometry (TOF-MS) on the electrolyte containing 10 mM TEMPO. Signals of the possible long-lived trapped radical intermediate were not observed in the mass spectrum (Figure S13). Room-temperature electron paramagnetic resonance (EPR) spectroscopy was conducted on BVO/TANF to further confirm the existence of short-lived radicals (Figure S14). The EPR spectra were collected under Xe lamp irradiation using 5,5-dimethyl-1-pyrroline N-oxide (DMPO) as the trapping agent. Signals of the radical intermediate were not detected after illumination in a 0.1 M Na_2SO_4/H_2SO_4 electrolyte (pH = 2) with 0.1 M glycerol and BVO/TANF. It is suggested that the PEC GOR on BVO/TANF is driven by holes rather than photogenerated hydroxyl radicals, as previously reported on a BVO photoanode.[11]

In situ FTIR spectroscopy was conducted on BVO and BVO/TANF NPs to study the molecular adsorption modes on different photoanodes. It is difficult to use glycerol directly because it is easily stuck to the catalyst and the lens of the IR cell as previously described in the prior report.[14] Hence, we choose 1-propanol and 2-propanol as the model molecules, which were widely used to distinguish the adsorption for primary and secondary hydroxyls in glycerol valorization.[48] Characteristic peaks of 1-propanol at 2970, 2886, 1392, and 1222 cm^{-1} were found on both BVO and BVO/TANF samples (Figure 5a), which corresponded to the methyl asymmetric

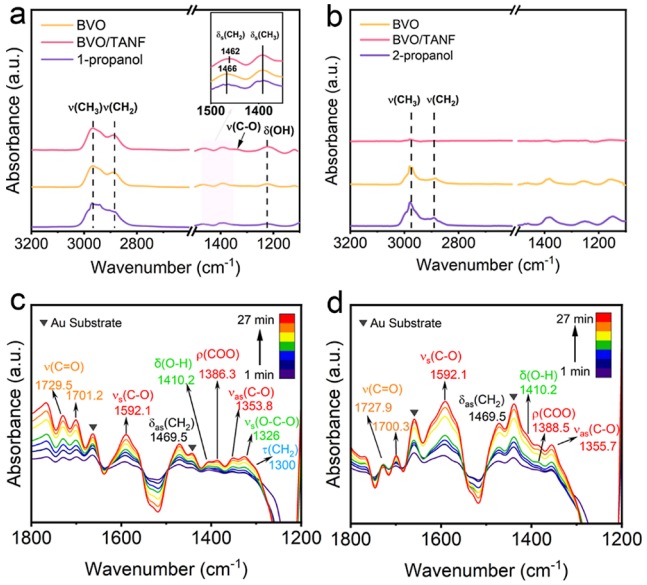

Figure 5. FTIR spectra of the BVO (yellow) and BVO/TANF (pink) NPs (a) after 1-propanol adsorption and (b) after 2-propanol adsorption with the characteristic band of alcohol molecules (purple). IRRAS of glycerol oxidation in (c) BVO and (d) BVO/TANF at 1.2 V *vs* RHE. The peaks of different species are displayed in the following colors: orange (DHA and other species containing carbonyl groups), red (FA), green (GLCA), and blue (GLA).

stretching vibration [$\nu(CH_3)_{as}$], symmetric stretching vibration [$\nu(CH_3)_s$], symmetrical deformation vibration [$\delta(CH_3)_s$], and O−H scissoring vibration [δ(OH)], respectively.[15] Nevertheless, compared to that for BVO, the adsorption band of symmetrical deformation vibration of methylene groups [$\delta(CH_2)_s$] shifted to a lower wavenumber on BVO/TANF (from 1466 to 1462 cm^{-1}). Meanwhile, a stronger peak located at 1353 cm^{-1} is shown in the spectra of BVO/TANF, which could be attributed to the C−O symmetric stretching [ν(CO)].[49] It was indicated that BVO/TANF has strong interaction with the hydroxyl and methylene groups in 1-propanol. A typical curve similar to that of the gas 2-propanol molecule was observed when 2-propanol was adsorbed on BVO (Figure 5b, yellow line). However, after the modification of the TANF catalyst, the magnitude of IR signals in the 2-propanol atmosphere was significantly decreased, which meant weak interaction between BVO/TANF and secondary hydroxyl. We also examined the adsorption band of BVO/TAN and BVO/TAF for 1-propanol and 2-propanol (Figure S15a,b). BVO/TAN displayed weak signals in the 2-propanol

https://doi.org/10.1021/acsami.2c20516
ACS Appl. Mater. Interfaces 2023, 15, 11678−11690

Scheme 2. Kinetics of the GOR on (a) BVO and (b) BVO/TANF

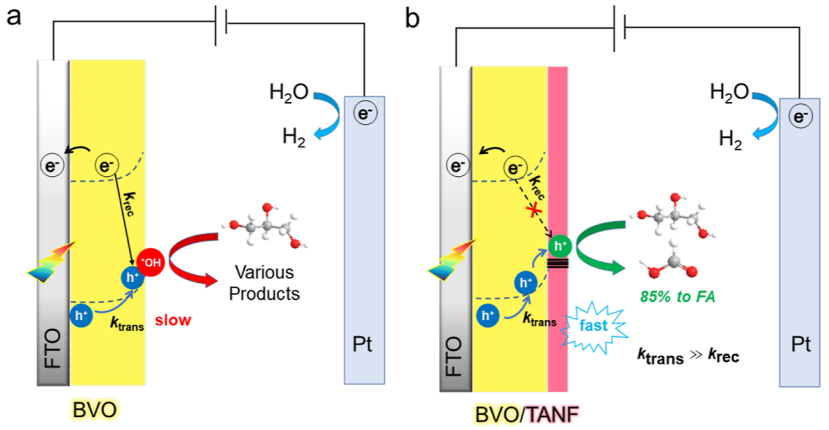

atmosphere like BVO/TANF, while BVO/TAF showed typical peaks of 2-propanol in the same atmosphere. The controlled trial of different modified NPs disclosed that nickel in the metal phenolic network makes the adsorption mode with primary hydroxyl in glycerol dominant on the BVO/TANF surface.

Although the *in situ* FTIR test implied that BVO/TANF could adsorb the primary hydroxyl of glycerol specifically, the reaction intermediates during the GOR need to be further detected to understand the different reaction pathways of BVO and BVO/TANF. Hence, we investigated the distinction of GOR kinetics on different samples through *in situ* IRRAS by tracking the formation of generated intermediates and products on the catalyst surface during the chronoamperometry measurement under visible light irradiation (Figures 5c,d and S15c,d). After the same period, BVO/TANF displays more intense signals than BVO on peaks at 1356, 1386−1389, and 1592 cm^{-1}, which can be assigned to the C−O symmetric stretching, COO rocking, and C−O asymmetric stretching of FA respectively,[49] indicating faster FA generation on the modified photoanode. In contrast to the evolutionary IR bands of FA, signals of GLCA (1326.0 and 1410.2 cm^{-1})[22,49,50] could hardly be observed on BVO/TANF, and the peak assigned to GLA was only observed in the spectrum collected at 1 min (1300.1 cm^{-1}). The peaks of GLA and GLCA were significant in the spectra of BVO instead (Figures 5c,d). The discrepancy of the GOR intermediate IR features suggests that photogenerated holes in BVO/TANF can break the C−C bonds of C2 and C3 intermediates more efficiently on the time scale that could not be captured by IRRAS. The vibrational bands at 1700−1800 cm^{-1} featuring the carbonyl groups manifest significantly declined signals in BVO/TANF compared to that for BVO (Figures 5c,d), supporting the elimination of aldehyde or ketone production. The collective results resolve the difference in GOR mechanisms between the modified and unmodified BVO photoanodes.

DISCUSSION

Charge Recombination and Hole Transfer Kinetics. The efficient kinetics give the GOR a clear advantage in achieving high photocurrents on BVO-based photoanodes in acidic conditions compared to that of the OER. As reported by a previous work, BVO displayed a low photocurrent of about 0.9 $mA{\cdot}cm^{-2}$ at 1.2 V *versus* RHE (pH = 2) with an onset potential of 0.7 V *versus* RHE for OER,[51] corresponding to our investigation (Figure 2b). The onset potential for the GOR is about 300 mV lower than that for the OER on BVO, indicating the favorable kinetics of the GOR in acidic conditions. Improved stability is also observed for the GOR on photoanodes compared to that for the OER (Figures 2c and S7b). Glycerol molecules have strong adhesion with the BVO surface,[11] which may prevent the photoanode from corrosion in acidic media. The effect of organic species in aqueous solution for prolonging the stability of BVO photoanodes has also been reported previously.[52−54] Since the organic species are more easily oxidized by photogenerated holes than water molecules, the photocorrosion of the BVO photoanode caused by holes is inhibited.[53] Still, the photocurrent of bare BVO is unfulfilled for the GOR (1.88 $mA{\cdot}cm^{-2}$ at 1.2 V *vs* RHE). The unsatisfactory photocurrent of BVO should be attributed to severe charge recombination according to prior reports.[40,55,56] A low η_{ct} was observed from bare BVO (44.8%, Figure 2d) for the GOR, indicating an over-half loss of holes due to surface recombination (Scheme 2a). After the modification of the NiFe phenolic networks, the charge recombination was significantly retarded with a much improved η_{ct} (86.5%, Figure 2d). The analysis of IMPS spectra provided adequate information about the charge recombination rate.[57−60] A k_{rec} value of 2.5×10^{-2} s^{-1} was observed on BVO/TANF at 1.2 V *versus* RHE, much lower than that on pristine BVO and the reported values on BVO-based photoanodes (0.1−10 s^{-1}).[57−60] The suppression of charge recombination was also revealed by the TPV/TPC technique with a slower recombination rate and a longer carrier lifetime on BVO/TANF (20.9 ms).[61] All these data suggest the effect of TANF in retarding charge recombination on the surface (Scheme 2b).

We also discovered that the TANF catalyst could speed up the photogenerated hole transfer from the bulk to substrate molecules in the BVO/TANF film. Compared to that of bare BVO, the improved τ_D and k_{trans} values of BVO/TANF calculated from the IMPS spectra indicated faster hole transfer (shown in Scheme 2a,b). A larger k_{trans}/k_{rec} ratio showed that hole transfer is much faster than charge recombination in BVO/TANF (Scheme 2a,b), leading to effective charge separation. The holes reaching the surface are then transferred from TANF to substrate molecules rapidly, as revealed by the low R_{ct} value (Scheme 2b).[62,63] The outstanding PEC performance of BVO/TANF is due to the retarded charge recombination, increased hole transfer rate, and sufficient utilization of photogenerated holes.

https://doi.org/10.1021/acsami.2c20516
ACS Appl. Mater. Interfaces 2023, 15, 11678−11690

Scheme 3. (a) Major Reaction Pathways on BVO and BVO/TANF. (b) Illustration of the GOR Taking Place on BVO/TANF

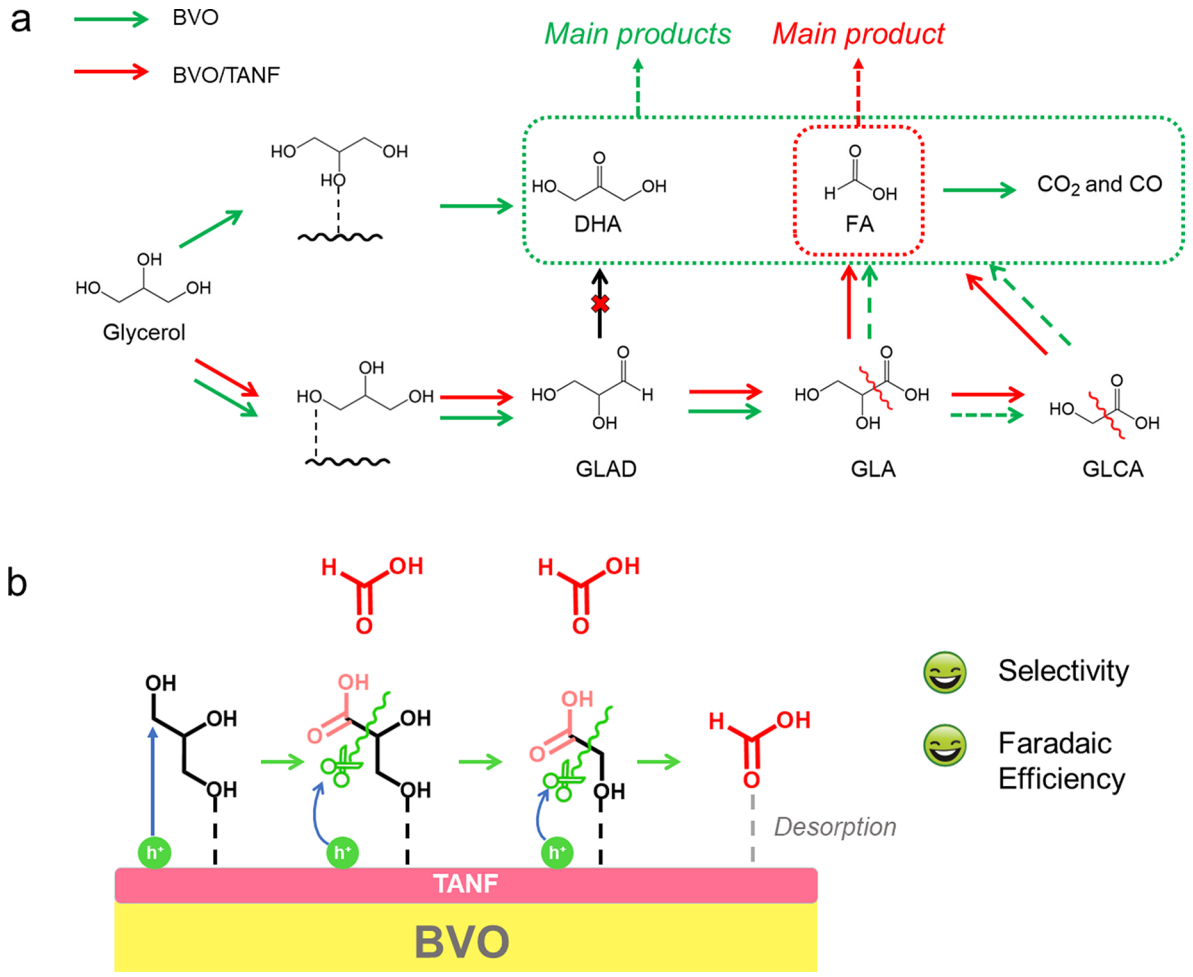

Catalytic Mechanism and Reaction Pathways. In the prior reports,[11,14,15] the GOR on semiconductor-based photoanodes in acidic conditions was found to be driven by hydroxyl radicals (shown in Scheme 2a). On bare BVO, the GOR could not fully consume the generated hydroxyl radicals. About 30% of electricity was used for excessive production of hydroxyl radicals and H_2O_2 accumulation.[11] The free H_2O_2 in the electrolyte would cause the overoxidation of organic molecules to CO_2.[15] However, our investigation indicated that photogenerated holes instead of hydroxyl radicals drive the GOR on the BVO/TANF photoanode. The quenching experiments showed that only the absence of holes would suppress FA production (Figure S12a,b). The results of TOF-MS and EPR further disprove that radical species are the intermediates for the GOR on BVO/TANF (Figures S13 and S14). Hence, we propose that the GOR is driven by holes on BVO/TANF (shown in Scheme 2b). The catalytic mechanism through photogenerated holes could avoid the accumulation of H_2O_2 and reach a high FE value toward liquid organic species.

Scheme 3a displays two typical PEC glycerol oxidation routines on the BVO surface: (i) glycerol → DHA (above) and (ii) glycerol → GLAD → GLA → GLCA → FA → CO_2 and/or CO (bottom). Since DHA, GLA, GLCA, and FA were all detected in product analysis for BVO and BVO/TANF, it is suggested that both BVO and BVO/TANF executed the two routes in parallel. The favorable route determined the main product of the GOR. Considering the high selectivity toward FA on BVO/TANF, the second routine should be dominant on BVO/TANF (Scheme 3b). According to prior reports, the bonding mode of glycerol on the electrode has a great impact on the GOR pathway.[15,64,65] The dominant adsorption mode to the primary alcohol in glycerol leads to the favorable generation of GLA, GLCA, or FA, while DHA is the main product if secondary alcohol is mainly absorbed on the electrode surface. As shown in the FTIR spectra of different photoanodes, primary alcohol and secondary alcohol could be largely adsorbed on bare BVO and BVO/TAF (Figure 5a,b). On the contrary, weak adsorption bands of 2-propanol (only containing secondary alcohol) were located on the FTIR spectra of BVO/TANF and BVO/TAN, which implied that the adsorption of primary alcohol was dominant (Figure 5a,b).

Given the high FE (over 94%) and similar adsorption mode of BVO/TAN and BVO/TANF, it is suggested that Ni sites in TANF and TAN may lead to the high selectivity toward FA. However, only a little enhancement of selectivity to FA was found on BVO/TAN compared to that on BVO (from 66.0 to 69.6%), lower than that on BVO/TANF (85%). The unsatisfied FA selectivity for BVO/TAN might be because of an insufficient Ni^{2+} load (revealed by XPS, Figure S5d), causing the modest generation of intermediate products GLA and GLCA (Figure 4a). After the addition of Fe^{2+} in the assembly of the metal phenolic co-catalyst, the intensity of Ni 2p peaks increased along with that of the O 1s and C 1s peaks (Figure S5e,f), suggesting that a thicker network with more

https://doi.org/10.1021/acsami.2c20516
ACS Appl. Mater. Interfaces 2023, 15, 11678−11690

immobilized Ni^{2+} ions was formed on BVO/TANF than on BVO/TAN. Moreover, the GLA and GLCA generated on Fe−phenol sites could be oxidized by nearby Ni sites since GLA and GLCA also have primary alcohols. The PEC oxidation currents of GLA and GLCA also supported this standpoint, where BVO/TANF displayed high current density toward the oxidation of both GLA and GLCA (Figure S16a). Low current density toward FA compared to that toward glycerol indicated the FA oxidation is unfavorable on BVO/TANF (Figure S16b). The full oxidation of C2−C3 products and inhibition of FA oxidation results in the highly selective conversion from glycerol to FA.

IRRAS further disclosed the GOR pathway on BVO/TANF. Bare BVO displayed strong absorbance on the peaks of carbonyl groups (Figure 5c), corresponding to the generation of DHA through routine (i) (Scheme 3a, upper solid green arrow). The absorption bonds with the modest intensity of GLA, GLCA, and FA were also detected on the spectra of BVO, which agreed with the incomplete conversion from GLA/GLCA to FA (Scheme 3a, lower dashed green arrows). Various products were obtained from the GOR with the unsatisfactory selectivity and FE (Scheme 3a, dashed green box). After the modification of TANF, the intensity of characteristic bands for DHA declined sharply, which indicated the unfavorable transformation from glycerol to DHA. The distinctive rise of IR peaks of FA on BVO/TANF was observed with the decreasing peak of GLA and weak signals of GLA as time went on (Figure 5d), indicating the fast transformation from GLA and GLCA to FA (solid red arrow in Scheme 3a). Thus, FA is detected as the main product with a high selectivity of 85% (Scheme 3a, red dashed box). The unique bonding mode, full conversion of C2−C3 intermediates, and retarded overoxidation of BVO/TANF result in highly selective FA generation on BVO/TANF (Scheme 3b).[66]

CONCLUSIONS

In summary, a NiFe−TA network overlayer (TANF) was combined with a nanoporous $BiVO_4$ (BVO) photoanode through *in situ* growth. In an acidic electrolyte, the modified photoanode (BVO/TANF) displayed a promising capability for transforming glycerol to FA under visible light irradiation. The FE reached ∼94% with a selectivity of 85% and a production rate of 573 mmol/(m^2·h) toward FA. The excellent PEC performance of BVO/TANF was due to the accelerated interfacial charge separation and retarded charge recombination kinetics. After the modification of the TANF co-catalyst on BVO, the charge transfer efficiency η_{ct} increased from 44.8 to 86.5%. Meanwhile, the charge recombination rate constant k_{rec} was calculated to be 2.5×10^{-2} s^{-1}, much lower than that in the previous report (0.1−10 s^{-1}) on BVO-based photoanodes. The favorable adsorption of primary alcohol on the TANF co-catalyst guided a high selectivity reaction pathway for glycerol oxidation toward FA. The efficient and selective photoanodic oxidation of biomass-derived glycerol provides a viable and smart alternative to the more challenging water oxidation in acidic media for the integration of PEC cells for solar energy conversion.

EXPERIMENTAL SECTION

Materials. All chemical reagents including $Bi(NO_3)_3·5H_2O$, $VO(acac)_2$, KI, nitric acid, 1,4-benzoquinone, hydrochloric acid, NaOH, $NiCl_2·6H_2O$, $FeCl_2·4H_2O$, NH_4VO_3, PEG-200, and TA were purchased from Adamas and used without further purification. The FTO electrodes (8 Ω/sq) were purchased from Suzhou Shangyang Solar Technology Co. Ltd. Prior to the electrochemical experiments, the FTO plates were cleaned by ultrasonication in deionized water, isopropanol, and ethanol (20 min), respectively.

Fabrication of BVO. BVO photoanodes were obtained according to the previous report[11,26] with little modification by thermal conversion of BiOI to BVO. A 0.04 M $Bi(NO_3)_3$ solution was prepared by dissolving $Bi(NO_3)_3·5H_2O$ in 50 mL of a 0.4 M KI solution after its pH was adjusted to 1.7 by adding HNO_3. This solution was mixed with 20 mL of absolute ethanol (100%) containing 0.23 M *p*-benzoquinone and was vigorously stirred for a few minutes. A typical three-electrode cell was used for electrodeposition. A 1 × 2 cm^2 FTO working electrode (WE), an Ag/AgCl (3 M KCl) reference electrode (RE), and a platinum counter electrode (CE) were used. A CHI760E potentiostat (Princeton Applied Research) was used for electrodeposition and subsequent electrochemical studies. Cathodic deposition of BiOI films was performed potentiostatically at −0.15 V *versus* Ag/AgCl under stirring at room temperature for 5 min. The obtained BiOI film was rinsed with deionized water and dried at room temperature. 0.2 mL of a DMSO solution containing 0.4 M vanadyl acetylacetonate [$VO(acac)_2$] was placed on the BiOI electrode (1 cm × 0.6 cm) and was annealed at 450 °C (ramping rate = 2 °C/min) for 2 h. Excess V_2O_5 present in the $BiVO_4$ electrodes was removed by soaking them in 1 M NaOH solution for 30 min with gentle stirring. The resulting pure BVO electrodes were rinsed with deionized (DI) water and dried at room temperature.

Fabrication of BVO/TANF. The TANF co-catalyst was loaded on BVO through a reported method with some modifications.[27] Briefly, a piece of the BVO photoanode (2 × 1 cm^2) was put in a 25 mL breaker with the BVO side facing down. 5 mL of 10 mM $FeCl_2$ and 5 mL of 10 mM $NiCl_2$ were added in this vessel. After full adsorption for ∼15 min, 10 mL of 9 mg L^{-1} TA solution was first added. 2 M NaOH was quickly added to the solution to change the pH to ∼8. Then, the vessel was shaken gently and stood without disturbance for 2 h. At last, the electrode with the product was washed with water several times and dried under ambient air.

Fabrication of BVO/TAN and BVO/TAF Photoanodes. The synthesis of BVO/TAN and BVO/TAF was similar to the routine of BVO/TANF with the only adjustment the composition of the metal ion solution, in which 10 mL of 10 mM $FeCl_2$ was used for BVO/TAF and 10 mL of $NiCl_2$ was used for BVO/TAN.

Fabrication of BVO NPs. The BVO NPs for FTIR and IRRAS tests were synthesized according to the previous report.[67] Bi $(NO_3)_3·5H_2O$ (15 mmol), NH_4VO_3 (15 mmol), and 20 mL polyethylene glycol with a molecular weight of 200 (PEG-200) were dissolved into 2 M HNO_3 solution (25 mL) and then magnetically stirred for 2 h. After adding 1.5 M NaOH (20 mL), the resulting solution was heated at 97 °C for 2 h. The solids obtained were washed with distilled water and then dried in a vacuum desiccator at room temperature. The particles were calcined at 500 °C in air for 1 h (ramping rate = 5 °C/min).

Fabrication of BVO/TANF NPs. The BVO/TANF NPs were synthesized by a similar pathway to that of BVO/TANF. 100 mg of BVO NPs was added to a 25 mL breaker with 5 mL of 10 mM $FeCl_2$ and 5 mL of 10 mM $NiCl_2$ solution and stirred for 15 min. Then, 10 mL of 9 mg L^{-1} TA solution was added, followed by 500 μL of 2 M NaOH. The mixture was stirred vigorously for 1 h, and 1 M HCl was added until the solution became transparent. The as-prepared BVO/TANF NPs were collected by centrifugation (10,000 rpm for 10 min), washed with water and ethanol successively, and vacuum-dried for 10 h.

Fabrication of BVO/TAN and BVO/TAF NPs. The synthesis of BVO/TAN and BVO/TAF NPs was similar to the routine of BVO/TANF with the only adjustment the composition of the metal ion solution, in which 10 mL of 10 mM $FeCl_2$ was used for BVO/TAF NPs and 10 mL of $NiCl_2$ was used for BVO/TAN NPs.

Characterization. The morphology and structure were examined by a ZEISS Gemini SEM 500 field-emission scanning electron microscope. TEM, HRTEM, EDX analysis, and STEM−EDS

https://doi.org/10.1021/acsami.2c20516
ACS Appl. Mater. Interfaces 2023, 15, 11678−11690

elemental mapping were carried out using an FEI Tecnai G2 F20 microscope. The XPS spectra were collected by a PHI5300. The XRD was carried out using a Bruker D2 PHASER. UV−vis diffuse reflectance spectra were collected on a Lambda 650S. ATR−FTIR spectra were collected by a Nicolet iS50 spectrometer.

PEC Characterization. LSV and $J-t$ tests were performed in a three-electrode electrochemical cell with a CHI760E instrument potentiostat (Shanghai Chenhua Instrument Co., Ltd.) at room temperature. In a three-electrode electrochemical system, the photoanodes were used as working electrodes, with an Ag/AgCl electrode (saturated KCl) as the reference electrode, and a platinum wire as the counter electrode. The visible light illumination was supplied by a Hecho S5000 LED lamp (65 W LED Cold Light Source, produced by Nanjing hecho technology co., ltd.), and the light intensity was calibrated to be 100 mW/cm^2 by a laser power meter (LP100, Changchun New Industries Optoelectronics Technology Co., Ltd.). All PEC measurements were conducted using back-side illumination (FTO|BVO side). Photocurrent density *versus* applied potential ($J-V$) curves were obtained by LSV with a scan rate of 10 mV/s. All measured potentials were converted to the RHE

$$E_{RHE} = E_{Ag/AgCl} + 0.197V + 0.0591 \times pH \quad (4)$$

Generally, for the GOR test, the electrolyte was 0.1 M Na_2SO_4 solution (30 mL, pH = 2) with 0.1 M glycerol. IPCE spectra were measured on a CIMPS system equipped with ZENNIUM X potentiostats, PP212 External potentiostats, and tunaable light sources (TLS03) (Zahner-Elektrik GmbH & Co. KG), and the IPCE values was calculated by

$$IPCE = \frac{\frac{1240}{\lambda} \times (J_{light} - J_{dark})}{P} \times 100\% \quad (5)$$

where λ is the wavelength, J_{light} is the photocurrent density under irradiation, J_{dark} is the current density under the dark condition, and P is the incident light power density. TPC and TPV measurements were conducted using a potentiostat (IM6ex, Zahner Company) controlled by a Zahner IMPS electrochemical workstation. The light was provided by a white LED (TLS01, Zahner-Elektrik GmbH & Co. KG), and the light intensity was set to 100 mW/cm^2. The TPC and TPV curves were analyzed by the following procedure. The decay curves were first normalized to the interval [0, 1] for TPC and TPV analysis. Then, the normalized data were fitted to a second-order exponential function as follows

$$y = y_0 + A_1 e^{-x/\tau_1} + A_2 e^{-x/\tau_2} \quad (6)$$

where τ_1 and τ_2 are the time constants and A_1 and A_2 are the probability constants. The percentage of τ_1 (φ_1) was calculated as

$$\varphi_1(\tau_1) = \frac{A_1}{(A_1 + A_2)} \times 100\% \quad (7)$$

and the percentage of τ_2 (φ_2) was calculated as

$$\varphi_2(\tau_2) = \frac{A_2}{(A_1 + A_2)} \times 100\% \quad (8)$$

The average decay time (τ) was calculated as

$$\overline{\tau} = \tau_1\varphi_1 + \tau_2\varphi_2 \quad (9)$$

IMPS measurements were conducted using a potentiostat (IM6ex, Zahner Company) controlled by a Zahner IMPS electrochemical workstation. Intensity-modulated light was provided by a white LED (TLS01, Zahner-Elektrik GmbH & Co. KG) that allowed the superimposition of sinusoidal modulation (~10%) at a DC illumination level. The average intensity of the visible light was 10 mW/cm^2. The photocurrent as a function of frequency (from 10 kHz to 0.1 Hz) was recorded at different potentials. The same three-electrode configuration and electrolyte were employed as those given above in the PEC Characterization section. EIS spectra was obtained in a 0.1 M Na_2SO_4 aqueous solution (pH 2) containing 0.1 M glycerol under the illumination of TLS 01 (light intensity of 100 mW/cm^2) over a frequency range from 4k to 0.1 Hz. The resulting data were fitted using the Zahner Analysis software.

Product Analysis. To quantitatively analyze the oxidation products, the PEC oxidation was performed in a cell containing 30 mL of the electrolyte with 0.1 M glycerol at a potential of 0.8 and 1.2 V *versus* RHE for 1 h. After the reaction, 0.5 mL of the solution was taken out from the cell and analyzed using HPLC to calculate the liquid product of glycerol conversion and yields of the products using an Agilent 1100 chromatograph equipped with a BioRad Aminex 87H column and a DAD detector. 5 mM H_2SO_4 solution was used as the mobile phase in the isocratic mode with a constant flow rate of 0.6 mL min^{-1}. The selectivity of FA was calculated based on

$$\text{selectivity (FA)} = \frac{n_{FA}}{n_{all}} \times 100\% = \frac{n_{FA}}{n_{FA} + n_{DHA} + n_{GLA} + n_{GLCA}} = \frac{c_{FA}}{c_{FA} + c_{DHA} + c_{GLA} + c_{GLCA}} \quad (10)$$

where n_{DHA}, n_{GLA}, n_{FA}, and n_{GLCA} are the yields of DHA, GLA, FA, and GLCA respectively, and c_{DHA}, c_{GLA}, c_{FA}, and c_{GLCA} are the concentrations of DHA, GLA, FA, and GLCA, respectively. The production rate per unit area of FA was calculated according to

$$\text{production rate per unit area (FA)} = \frac{c_{FA} \times V}{t \times A} \quad (11)$$

where V is the volume of the reaction solution, t is the reaction time, and A is the area of the photoanode. Calculations of FEs of the PEC glycerol oxidation based on the following balanced half-reactions corresponded to the conversion of glycerol into the individual GOR product in the acidic solution

$$C_3H_8O_3\ (\text{glycerol}) \rightarrow C_3H_6O_3\ (\text{DHA}) + 2H^+ + 2e^- \quad (12)$$

$$C_3H_8O_3\ (\text{glycerol}) + H_2O \rightarrow C_3H_6O_4\ (\text{GLA}) + 4H^+ + 4e^- \quad (13)$$

$$C_3H_8O_3\ (\text{glycerol}) + \frac{3}{2}H_2O \rightarrow \frac{3}{2}C_2H_4O_3\ (\text{GLCA}) + 5H^+ + 5e^- \quad (14)$$

$$C_3H_8O_3\ (\text{glycerol}) + 3H_2O \rightarrow 3HCOOH\ (\text{FA}) + 8H^+ + 8e^- \quad (15)$$

Hence, the overall FE toward all value-added products is calculated by

$$FE\ (\text{all}) = \frac{c_{FA} \times \frac{8}{3} + c_{DHA} \times 2 + c_{GLA} \times 4 + c_{GLCA} \times \frac{10}{3}}{Q_{total}} \times V \times F \times 100\% \quad (16)$$

The evolved hydrogen was measured using a gas chromatograph 9790 Plus (Zhejiang Fuli Analytical Instruments Inc.) using a thermal conductivity detector and a flame ionization detector. Argon was used as the carrier gas. Before the measurement, the electrolyte was degassed by bubbling with high-purity Ar for 30 min. The FE was calculated by assuming that all of the charges were caused by 2e$^-$ reduction of the proton to produce H_2.

Electron Spin Resonance Measurements. Electron spin resonance (ESR) spectra of BVO/TANF NPs were collected on a Bruker EMXplus-6/1 ESR spectrometer (300 K, 9.823 GHz, X-band). The microwave power employed was 6.325 mW. The sweep width was set to 100.0 G. The modulation frequency and modulation amplitude were 100k GHz and 1.000 GHz, respectively. DMPO was used as the spin-trapping agent. 0.5 mg of the BVO/TANF photocatalyst was dispersed in 2 mL of the 0.1 M Na_2SO_4 electrolyte (pH = 2) with or without 0.1 M glycerol, and then, 60 μL of the DMPO aqueous solution (0.2 M) was added into the solution for ESR measurement. Then, the sample was irradiated by a Xe lamp (100 mW·cm-2) at different times.

https://doi.org/10.1021/acsami.2c20516
ACS Appl. Mater. Interfaces 2023, 15, 11678−11690

***In situ* FTIR Tests.** *In situ* FTIR spectra for investigating the adsorption of 1-propanol and 2-propanol on the surface of the BVO and BVO/TANF NPs were recorded on a Nicolet 6700 spectrometer equipped with a cell fitted with CaF_2 windows and an MCT-A detector cooled with liquid nitrogen. The spectrum was collected at a resolution of 4 cm^{-1} with an accumulation of 64 scans in the range of 4000−1100 cm^{-1}. The sample was pretreated under a flow of Ar for 40 min at 200 °C to remove the impurities absorbed on the surface and then cooled to 20 °C. The background was collected at 20 °C under a flow of Ar. 1-Propanol or 2-propanol was bubbled into the sample by a flow of Ar at 20 °C for 20 min to obtain a stable spectrum. Then, the system was purged with a flow of Ar to remove physical adsorption and collect the spectrum after the spectrum was stable.

IRRAS Tests. IRRAS measurements were conducted on a Nicolet 6700 spectrometer equipped with a cell fitted with CaF_2 windows and an MCT-A detector cooled with liquid nitrogen. Before the IRRAS test, Au film electrodes plated on Si were prepared first. The plating solution for Au deposition was obtained by mixing solution A (0.1222 g of NaOH and 0.2286 g of $NaAuCl_4{\cdot}2H_2O$ dissolved in 3 mL of DI water) and solution B (0.134 g of NH_4Cl, 0.9468 g of Na_2SO_3, and 0.6202 g of $NaS_2O_3{\cdot}5H_2O$ dissolved in 50 mL of DI water) along with 50 mL of DI water and sonicating for 2 h. The prism used was a non-doped Si hemicylinder [Linglu Instrument (Shanghai) Co., Ltd]. The reflecting plane of the prism on which metal is deposited was polished with successively finer grade alumina slurries down to 0.05 μm, followed by sonication in acetone and then water. Then, the surface was immersed in a solution of $V_{H_2SO_4}/V_{H_2O_2}$ = 3:1 for 20 min and rinsed with DI water. The surface was contacted with 40% NH_4F for several minutes to remove the oxide layer on the Si surface and to terminate it with hydrogen. Deposition of Au was performed by immersing the Si surface in 15 mL of plating solution for 4−5 min, which was pre-heated at 50−55 °C with 3.4 mL of 2% HF solution. The obtained Si prism coated with the Au film was rinsed with DI water for 2 min for later use. BVO/TANF and BVO NPs were drop-casted on the Au film. IR spectra were collected in a custom-made cell [Linglu Instrument (Shanghai) Co., Ltd] containing 30 mL of the electrolyte with 0.1 M glycerol at a potential of 1.2 V *versus* RHE for 30 min under LED irradiation.

■ ASSOCIATED CONTENT

Supporting Information

The Supporting Information is available free of charge at https://pubs.acs.org/doi/10.1021/acsami.2c20516.

Additional electrochemical, spectral, and microscopic characterizations for different photoanodes; product analysis for different photoanodes; and scavenger quenching experiments, TOF-MS spectra, and room-temperature ESR spectra for intermediate determination (PDF)

■ AUTHOR INFORMATION

Corresponding Author

Ke Hu − *Department of Chemistry, Fudan University, Shanghai 200433, P. R. China;* orcid.org/0000-0002-0240-7192; Email: khu@fudan.edu.cn

Authors

Yiming Han − *Department of Chemistry, Fudan University, Shanghai 200433, P. R. China*

Mingwei Chang − *College of Mathematics and Physics, Shanghai University of Electric Power, Shanghai 201306, China*

Zijian Zhao − *Department of Chemistry, Fudan University, Shanghai 200433, P. R. China*

Fushuang Niu − *Department of Chemistry, Fudan University, Shanghai 200433, P. R. China*

Zhenghao Zhang − *Department of Chemistry, Fudan University, Shanghai 200433, P. R. China*

Zehui Sun − *Department of Chemistry, Fudan University, Shanghai 200433, P. R. China*

Liming Zhang − *Department of Chemistry, Fudan University, Shanghai 200433, P. R. China;* orcid.org/0000-0001-6795-3381

Complete contact information is available at: https://pubs.acs.org/10.1021/acsami.2c20516

Notes

The authors declare no competing financial interest.

■ ACKNOWLEDGMENTS

This work was sponsored by the National Natural Science Foundation of China (21872037 and 22173022) and Natural Science Foundation of Shanghai (21ZR1404400)

■ REFERENCES

(1) Xia, C.; Li, Y.; Je, M.; Kim, J.; Cho, S. M.; Choi, C. H.; Choi, H.; Kim, T.-H.; Kim, J. K. Nanocrystalline Iron Pyrophosphate-Regulated Amorphous Phosphate Overlayer for Enhancing Solar Water Oxidation. *Nano-Micro Lett.* **2022**, *14*, 209.

(2) Li, Y.; Je, M.; Kim, J.; Xia, C.; Roh, S. H.; So, W.; Lee, H.; Kim, D.-H.; Cho, S. M.; Bae, J. W.; Choi, H. J. K.; Kim, J. K. Rational Nanopositioning of Homogeneous Amorphous Phase on Crystalline Tungsten Oxide for Boosting Solar Water Oxidation. *Chem. Eng. J.* **2022**, *438*, 135532.

(3) Seabold, J. A.; Choi, K.-S. Efficient and Stable Photo-Oxidation of Water by a Bismuth Vanadate Photoanode Coupled with an Iron Oxyhydroxide Oxygen Evolution Catalyst. *J. Am. Chem. Soc.* **2012**, *134*, 2186−2192.

(4) Walter, M. G.; Warren, E. L.; McKone, J. R.; Boettcher, S. W.; Mi, Q. X.; Santori, E. A.; Lewis, N. S. Solar Water Splitting Cells. *Chem. Rev.* **2010**, *110*, 6446−6473.

(5) Meyer, T. J. Catalysis: the Art of Splitting Water. *Nature* **2008**, *451*, 778−779.

(6) Lewis, N. S.; Nocera, D. G. Powering the Planet: Chemical Challenges in Solar Energy Utilization. *Proc. Natl. Acad. Sci. U.S.A.* **2006**, *103*, 15729−15735.

(7) Nguyen, D. N.; Gund, G. S.; Jung, M. G.; Roh, S. H.; Park, J.; Kim, J. K.; Park, H. S. Core-Shell Structured MXene@Carbon Nanodots as Bifunctional Catalysts for Solar-Assisted Water Splitting. *ACS Nano* **2020**, *14*, 17615−17625.

(8) Toldrá-Reig, F.; Mora, L.; Toldrá, F. Trends in Biodiesel Production from Animal Fat Waste. *Appl. Sci.* **2020**, *10*, 3644.

(9) Behr, A.; Eilting, J.; Irawadi, K.; Leschinski, J.; Lindner, F. Improved Utilisation of Renewable Resources: New Important Derivatives of Glycerol. *Green Chem.* **2008**, *10*, 13−30.

(10) Fan, L.; Liu, B.; Liu, X.; Senthilkumar, N.; Wang, G.; Wen, Z. Recent Progress in Electrocatalytic Glycerol Oxidation. *Energy Technol.* **2020**, *9*, 2000804.

(11) Liu, D.; Liu, J. C.; Cai, W.; Ma, J.; Yang, H. B.; Xiao, H.; Li, J.; Xiong, Y.; Huang, Y.; Liu, B. Selective Photoelectrochemical Oxidation of Glycerol to High Value-Added Dihydroxyacetone. *Nat. Commun.* **2019**, *10*, 1779.

(12) Ke, Z. J.; Williams, N.; Yan, X. X.; Younan, S.; He, D.; Song, X. Y.; Pan, X. Q.; Xiao, X. H.; Gu, J. Solar-Assisted Co-Electrolysis of Glycerol and Water for Concurrent Production of Formic Acid and Hydrogen. *J. Mater. Chem. A* **2021**, *9*, 19975−19983.

(13) Lee, Y.; Kim, S.; Jeong, S. Y.; Seo, S.; Kim, C.; Yoon, H.; Jang, H. W.; Lee, S. Surface-Modified Co-doped ZnO Photoanode for Photoelectrochemical Oxidation of Glycerol. *Catal. Today* **2021**, *359*, 43−49.

(14) Liu, Y.; Wang, M.; Zhang, B.; Yan, D. P.; Xiang, X. Mediating the Oxidizing Capability of Surface-Bound Hydroxyl Radicals Produced by Photoelectrochemical Water Oxidation to Convert Glycerol into Dihydroxyacetone. *ACS Catal.* **2022**, *12*, 6946−6957.
(15) Luo, L.; Chen, W.; Xu, S. M.; Yang, J.; Li, M.; Zhou, H.; Xu, M.; Shao, M.; Kong, X.; Li, Z.; Duan, H. Selective Photoelectrocatalytic Glycerol Oxidation to Dihydroxyacetone via Enhanced Middle Hydroxyl Adsorption over a Bi_2O_3-Incorporated Catalyst. *J. Am. Chem. Soc.* **2022**, *144*, 7720−7730.
(16) Wang, Q.; Ma, X.; Wu, P.; Li, B.; Zhang, L.; Shi, J. CoNiFe-LDHs Decorated Ta_3N_5 Nanotube Array Photoanode for Remarkably Enhanced Photoelectrochemical Glycerol Conversion Coupled with Hydrogen Generation. *Nano Energy* **2021**, *89*, 106326.
(17) Bruggeman, D. F.; Laporte, A. A. H.; Detz, R. J.; Mathew, S.; Reek, J. N. H. Aqueous Biphasic Dye-Sensitized Photosynthesis Cells for TEMPO-Based Oxidation of Glycerol. *Angew. Chem., Int. Ed.* **2022**, *61*, No. e202200175.
(18) Reier, T.; Nong, H. N.; Teschner, D.; Schlögl, R.; Strasser, P. Electrocatalytic Oxygen Evolution Reaction in Acidic Environments - Reaction Mechanisms and Catalysts. *Adv. Energy Mater.* **2017**, *7*, 1601275.
(19) Luo, H.; Barrio, J.; Sunny, N.; Li, A.; Steier, L.; Shah, N. I.; Stephens, I. E. L.; Titirici, M. M. Progress and Perspectives in Photo- and Electrochemical-Oxidation of Biomass for Sustainable Chemicals and Hydrogen Production. *Adv. Energy Mater.* **2021**, *11*, 2101180.
(20) Tateno, H.; Chen, S. Y.; Miseki, Y.; Nakajima, T.; Mochizuki, T.; Sayama, K. Photoelectrochemical Oxidation of Glycerol to Dihydroxyacetone Over an Acid-Resistant Ta:BiVO4 Photoanode. *ACS Sustainable Chem. Eng.* **2022**, *10*, 7586−7594.
(21) Li, Y.; Wei, X.; Chen, L.; Shi, J.; He, M. Nickel-molybdenum Nitride Nanoplate Electrocatalysts for Concurrent Electrolytic Hydrogen and Formate Productions. *Nat. Commun.* **2019**, *10*, 5335.
(22) Wu, J.; Li, J.; Li, Y.; Ma, X. Y.; Zhang, W. Y.; Hao, Y.; Cai, W. B.; Liu, Z. P.; Gong, M. Steering the Glycerol Electro-Reforming Selectivity via Cation-Intermediate Interactions. *Angew. Chem., Int. Ed.* **2022**, *61*, No. e202113362.
(23) Han, X. T.; Sheng, H. Y.; Yu, C.; Walker, T. W.; Huber, G. W.; Qiu, J. S.; Jin, S. Electrocatalytic Oxidation of Glycerol to Formic Acid by CuCo2O4 Spinel Oxide Nanostructure Catalysts. *ACS Catal.* **2020**, *10*, 6741−6752.
(24) Huang, Z. F.; Pan, L.; Zou, J. J.; Zhang, X.; Wang, L. Nanostructured Bismuth Vanadate-Based Materials For Solar-Energy-Driven Water Oxidation: A Review On Recent Progress. *Nanoscale* **2014**, *6*, 14044−14063.
(25) Wu, Y.-H.; Kuznetsov, D. A.; Pflug, N. C.; Fedorov, A.; Müller, C. R. Solar-driven Valorisation of Glycerol on $BiVO_4$ Photoanodes: Effect of Co-Catalyst and Reaction Media on Reaction Selectivity. *J. Mater. Chem. A* **2021**, *9*, 6252−6260.
(26) Kim, T. W.; Choi, K. S. Nanoporous $BiVO_4$ Photoanodes with Dual-Layer Oxygen Evolution Catalysts for Solar Water Splitting. *Science* **2014**, *343*, 990−994.
(27) Shi, Y. M.; Yu, Y. F.; Yu, Y.; Huang, Y.; Zhao, B. H.; Zhang, B. Boosting Photoelectrochemical Water Oxidation Activity and Stability of Mo-Doped $BiVO_4$ through the Uniform Assembly Coating of NiFe-Phenolic Networks. *ACS Energy Lett.* **2018**, *3*, 1648−1654.
(28) Cao, X.; Xu, C.; Liang, X.; Ma, J.; Yue, M.; Ding, Y. Rationally Designed/assembled Hybrid $BiVO_4$-Based Photoanode for Enhanced Photoelectrochemical Performance. *Appl. Catal., B* **2020**, *260*, 118136.
(29) Ejima, H.; Richardson, J. J.; Liang, K.; Best, J. P.; van Koeverden, M. P.; Such, G. K.; Cui, J.; Caruso, F. One-step Assembly of Coordination Complexes for Versatile Film and Particle Engineering. *Science* **2013**, *341*, 154−157.
(30) Qiu, H.; Ni, W.; Yang, L.; Zhang, Q. Remarkable Ability of Pb(II) Capture from Water by Self-assembled Metal-Phenolic Networks Prepared with Tannic Acid and Ferric Ions. *Chem. Eng. J.* **2022**, *450*, 138161.
(31) Xiao, Y.; Guo, D.; Li, T.; Zhou, Q.; Shen, L.; Li, R.; Xu, Y.; Lin, H. Facile Fabrication of Superhydrophilic Nanofiltration Membranes via Tannic Acid And Irons Layer-By-Layer Self-Assembly for Dye Separation. *Appl. Surf. Sci.* **2020**, *515*, 146063.
(32) Cui, J.; Ren, S.; Lin, T.; Feng, Y.; Jia, S. Shielding Effects of Fe^{3+}-Tannic Acid Nanocoatings for Immobilized Enzyme on Magnetic Fe_3O_4@Silica Core Shell Nanosphere. *Chem. Eng. J.* **2018**, *343*, 629−637.
(33) Wang, S.; Chen, P.; Bai, Y.; Yun, J.-H.; Liu, G.; Wang, L. New $BiVO_4$ Dual Photoanodes with Enriched Oxygen Vacancies for Efficient Solar-Driven Water Splitting. *Adv. Mater.* **2018**, *30*, 1800486.
(34) Pan, J. B.; Wang, B. H.; Wang, J. B.; Ding, H. Z.; Zhou, W.; Liu, X.; Zhang, J. R.; Shen, S.; Guo, J. K.; Chen, L.; Au, C. T.; Jiang, L. L.; Yin, S. F. Activity and Stability Boosting of an Oxygen-Vacancy-Rich $BiVO_4$ Photoanode by NiFe-MOFs Thin Layer for Water Oxidation. *Angew. Chem., Int. Ed.* **2021**, *60*, 1433−1440.
(35) Tachan, Z.; Hod, I.; Zaban, A. The TiO_2-Catechol Complex: Coupling Type II Sensitization with Efficient Catalysis of Water Oxidation. *Adv. Energy Mater.* **2014**, *4*, 1301249.
(36) Nesbitt, H. W.; Legrand, D.; Bancroft, G. M. Interpretation of Ni2p XPS Spectra of Ni Conductors and Ni Insulators. *Phys. Chem. Miner.* **2000**, *27*, 357−366.
(37) Biesinger, M. C.; Lau, L. W. M.; Gerson, A. R.; Smart, R. S. C. The Role of the Auger Parameter in XPS Studies of Nickel Metal, Halides and Oxides. *Phys. Chem. Chem. Phys.* **2012**, *14*, 2434−2442.
(38) Shi, Y.; Yu, Y.; Liang, Y.; Du, Y.; Zhang, B. In Situ Electrochemical Conversion of an Ultrathin Tannin Nickel Iron Complex Film as an Efficient Oxygen Evolution Reaction Electrocatalyst. *Angew. Chem., Int. Ed.* **2019**, *58*, 3769−3773.
(39) Zhang, W.; Besford, Q. A.; Christofferson, A. J.; Charchar, P.; Richardson, J. J.; Elbourne, A.; Kempe, K.; Hagemeyer, C. E.; Field, M. R.; McConville, C. F.; Yarovsky, I.; Caruso, F. Cobalt-Directed Assembly of Antibodies onto Metal-Phenolic Networks for Enhanced Particle Targeting. *Nano Lett.* **2020**, *20*, 2660−2666.
(40) Zachäus, C.; Abdi, F. F.; Peter, L. M.; van de Krol, R. Photocurrent of $BiVO_4$ is Limited by Surface Recombination, not Surface Catalysis. *Chem. Sci.* **2017**, *8*, 3712−3719.
(41) Ponomarev, E. A.; Peter, L. M. A Generalized Theory of Intensity Modulated Photocurrent Spectroscopy (IMPS). *J. Electroanal. Chem.* **1995**, *396*, 219−226.
(42) Klotz, D.; Ellis, D. S.; Dotan, H.; Rothschild, A. Empirical in Operando Analysis of the Charge Carrier Dynamics in Hematite Photoanodes by PEIS, IMPS and IMVS. *Phys. Chem. Chem. Phys.* **2016**, *18*, 23438−23457.
(43) Li, W.; He, D.; Sheehan, S. W.; He, Y.; Thorne, J. E.; Yao, X.; Brudvig, G. W.; Wang, D. Comparison of Heterogenized Molecular and Heterogeneous Oxide Catalysts for Photoelectrochemical Water Oxidation. *Energy Environ. Sci.* **2016**, *9*, 1794−1802.
(44) Li, L.; Li, J.; Bai, J.; Zeng, Q.; Xia, L.; Zhang, Y.; Chen, S.; Xu, Q.; Zhou, B. Serial Hole Transfer Layers for a $BiVO_4$ Photoanode with Enhanced Photoelectrochemical Water Splitting. *Nanoscale* **2018**, *10*, 18378−18386.
(45) Xia, L.; Li, J.; Bai, J.; Li, L.; Chen, S.; Zhou, B. $BiVO_4$ Photoanode with Exposed (040) Facets for Enhanced Photoelectrochemical Performance. *Nano-Micro Lett.* **2017**, *10*, 11.
(46) Liu, Y.; Xia, M.; Yao, L.; Mensi, M.; Ren, D.; Grätzel, M.; Sivula, K.; Guijarro, N. Spectroelectrochemical and Chemical Evidence of Surface Passivation at Zinc Ferrite ($ZnFe_2O_4$) Photoanodes for Solar Water Oxidation. *Adv. Funct. Mater.* **2021**, *31*, 2010081.
(47) Xu, W.; Tian, W.; Li, L. Two-Dimentional Nanostructured Metal Oxide/Sulfide-Based Photoanode for Photoelectrochemical Water Splitting. *Sol. RRL* **2021**, *5*, 2000412.
(48) An, Z.; Ma, H. H.; Han, H. B.; Huang, Z. Y.; Jiang, Y. T.; Wang, W. L.; Zhu, Y. R.; Song, H. Y.; Shu, X.; Xiang, X.; He, J. Insights into the Multiple Synergies of Supports in the Selective Oxidation of Glycerol to Dihydroxyacetone: Layered Double Hydroxide Supported Au. *ACS Catal.* **2020**, *10*, 12437−12453.
(49) He, Z.; Hwang, J.; Gong, Z.; Zhou, M.; Zhang, N.; Kang, X.; Han, J. W.; Chen, Y. Promoting Biomass Electrooxidation via

Modulating Proton and Oxygen Anion Deintercalation in Hydroxide. *Nat. Commun.* **2022**, *13*, 3777.
(50) Kondamudi, N.; Misra, M.; Banerjee, S.; Mohapatra, S.; Mohapatra, S. Simultaneous Production of Glyceric Acid and Hydrogen from the Photooxidation of Crude Glycerol Using $TiSi_2$. *Appl. Catal., B* **2012**, *126*, 180−185.
(51) Murakami, T.; Ikezoi, K.; Nagai, K.; Kato, H.; Abe, T. A Water-Splitting System with a Cobalt (II,III) Oxide Co-Catalyst-Loaded Bismuth Vanadate Photoanode Along with an Organo-Photocathode. *ChemElectroChem* **2020**, *7*, 5029−5035.
(52) Wang, Z.; Guo, Y.; Liu, M.; Liu, X.; Zhang, H.; Jiang, W.; Wang, P.; Zheng, Z.; Liu, Y.; Cheng, H.; Dai, Y.; Wang, Z.; Huang, B. Boosting H2 Production from a BiVO4 Photoelectrochemical Biomass Fuel Cell by the Construction of a Bridge for Charge and Energy Transfer. *Adv. Mater.* **2022**, *34*, 2201594.
(53) Zhang, S.; Rohloff, M.; Kasian, O.; Mingers, A. M.; Mayrhofer, K. J. J.; Fischer, A.; Scheu, C.; Cherevko, S. Dissolution of $BiVO_4$ Photoanodes Revealed by Time-Resolved Measurements under Photoelectrochemical Conditions. *J. Phys. Chem. C* **2019**, *123*, 23410−23418.
(54) Nakajima, T.; Miseki, Y.; Tateno, H.; Tsuchiya, T.; Sayama, K. Acid-Resistant BiVO4 Photoanodes: Insolubility Control by Solvents and Weak W Diffusion in the Lattice. *ACS Appl. Mater. Interfaces* **2021**, *13*, 12079−12090.
(55) Ma, Y. M.; Pendlebury, S. R.; Reynal, A.; Le Formal, F.; Durrant, J. R. Dynamics of photogenerated holes in undoped BiVO4 photoanodes for solar water oxidation. *Chem. Sci.* **2014**, *5*, 2964−2973.
(56) Ma, Y. M.; Kafizas, A.; Pendlebury, S. R.; Le Formal, F.; Durrant, J. R. Photoinduced Absorption Spectroscopy of CoPi on $BiVO_4$: The Function of CoPi during Water Oxidation. *Adv. Funct. Mater.* **2016**, *26*, 4951−4960.
(57) Yu, F.; Li, F.; Yao, T.; Du, J.; Liang, Y.; Wang, Y.; Han, H.; Sun, L. Fabrication and Kinetic Study of a Ferrihydrite-Modified $BiVO_4$ Photoanode. *ACS Catal.* **2017**, *7*, 1868−1874.
(58) Antuch, M.; Millet, P.; Iwase, A.; Kudo, A. The Role of Surface States During Photocurrent Switching: Intensity Modulated Photocurrent Spectroscopy Analysis of $BiVO_4$ Photoelectrodes. *Appl. Catal., B* **2018**, *237*, 401−408.
(59) Liu, Y.; Jiang, Y.; Li, F.; Yu, F.; Jiang, W.; Xia, L. Molecular Cobalt Salophen Catalyst-Integrated $BiVO_4$ as Stable and Robust Photoanodes for Photoelectrochemical Water Splitting. *J. Mater. Chem. A* **2018**, *6*, 10761−10768.
(60) Tian, Z.; Zhang, P.; Qin, P.; Sun, D.; Zhang, S.; Guo, X.; Zhao, W.; Zhao, D.; Huang, F. Novel Black $BiVO_4/TiO_{2-x}$ Photoanode with Enhanced Photon Absorption and Charge Separation for Efficient and Stable Solar Water Splitting. *Adv. Energy Mater.* **2019**, *9*, 1901287.
(61) Niu, F.; Zhou, Q.; Han, Y.; Liu, R.; Zhao, Z.; Zhang, Z.; Hu, K. Rapid Hole Extraction Based on Cascade Band Alignment Boosts Photoelectrochemical Water Oxidation Efficiency. *ACS Catal.* **2022**, *12*, 10028−10038.
(62) Iwami, H.; Okamura, M.; Kondo, M.; Masaoka, S. Electrochemical Polymerization Provides a Function-Integrated System for Water Oxidation. *Angew. Chem., Int. Ed.* **2021**, *60*, 5965−5969.
(63) Kan, M.; Xue, D.; Jia, A.; Qian, X.; Yue, D.; Jia, J.; Zhao, Y. A Highly Efficient Nanoporous $BiVO_4$ Photoelectrode with Enhanced Interface Charge Transfer Co-Catalyzed By Molecular Catalyst. *Appl. Catal., B* **2018**, *225*, 504−511.
(64) Garcia, A. C.; Kolb, M. J.; van Nierop y Sanchez, C.; Vos, J.; Birdja, Y. Y.; Kwon, Y.; Tremiliosi-Filho, G.; Koper, M. T. M. Strong Impact of Platinum Surface Structure on Primary and Secondary Alcohol Oxidation during Electro-Oxidation of Glycerol. *ACS Catal.* **2016**, *6*, 4491−4500.
(65) Kwon, Y.; Schouten, K. J. P.; Koper, M. T. M. Mechanism of the Catalytic Oxidation of Glycerol on Polycrystalline Gold and Platinum Electrodes. *ChemCatChem* **2011**, *3*, 1176−1185.
(66) Wang, Y.; Zhu, Y.-Q.; Xie, Z.; Xu, S.-M.; Xu, M.; Li, Z.; Ma, L.; Ge, R.; Zhou, H.; Li, Z.; Kong, X.; Zheng, L.; Zhou, J.; Duan, H. Efficient Electrocatalytic Oxidation of Glycerol via Promoted OH* Generation over Single-Atom-Bismuth-Doped Spinel Co_3O_4. *ACS Catal.* **2022**, *12*, 12432−12443.
(67) Eda, S.-i.; Fujishima, M.; Tada, H. Low Temperature-Synthesis of $BiVO_4$ Nanorods Using Polyethylene Glycol As a Soft Template and the Visible-light-activity for Copper Acetylacetonate Decomposition. *Appl. Catal., B* **2012**, *125*, 288−293.

https://doi.org/10.1021/acsami.2c20516
ACS Appl. Mater. Interfaces 2023, 15, 11678−11690